PAPER

Infiltration of tumor spheroids by activated immune cells

View the article online for updates and enhancements.

Physical Biology

PAPER

Infiltration of tumor spheroids by activated immune cells

Mrinmoy Mukherjee[1,*] [ID], **Oleksandr Chepizhko**[2,3] [ID], **Maria Chiara Lionetti**[4] [ID], **Stefano Zapperi**[5,6] [ID], **Caterina A M La Porta**[4,7] [ID] **and Herbert Levine**[1,8] [ID]

1 Center for Theoretical Biological Physics, Northeastern University, Boston, MA, United States of America
2 Institut für Theoretische Physik, Leopold-Franzens-Universität Innsbruck, Technikerstrasse 21a, A-6020 Innsbruck, Austria
3 Institute of Mathematics and Statistics, University of Tartu, Tartu, Estonia
4 Center for Complexity and Biosystems, Department of Environmental Science and Policy, University of Milan, via Celoria 10, 20133 Milano, Italy
5 Center for Complexity and Biosystems, Department of Physics, University of Milan, via Celoria 16, 20133 Milano, Italy
6 CNR—Consiglio Nazionale delle Ricerche, Istituto di Chimica della Materia Condensata e di Tecnologie per l'Energia, Lecco, Italy
7 CNR—Consiglio Nazionale delle Ricerche, Istituto di Biofisica, via Via De Marini 6, 16149 Genova, Italy
8 Department of Physics and Bioengineering, Northeastern University, Boston, MA, United States of America
* Author to whom any correspondence should be addressed.

E-mail: mr.mukherjee@northeastern.edu

Abstract

Recent years have seen a tremendous growth of interest in understanding the role that the adaptive immune system could play in interdicting tumor progression. In this context, it has been shown that the density of adaptive immune cells inside a solid tumor serves as a favorable prognostic marker across different types of cancer. The exact mechanisms underlying the degree of immune cell infiltration is largely unknown. Here, we quantify the temporal dynamics of the density profile of activated immune cells around a solid tumor spheroid. We propose a computational model incorporating immune cells with active, persistent movement and a proliferation rate that depends on the presence of cancer cells, and show that the model able to reproduce semi-quantitatively the experimentally measured infiltration profile. Studying the density distribution of immune cells inside a solid tumor can help us better understand immune trafficking in the tumor micro-environment, hopefully leading towards novel immunotherapeutic strategies.

1. Introduction

The destruction of cancer cells by the immune system is the primary objective of immunotherapy [1–4]. Despite consistent progress in immune oncology by different techniques such as checkpoint inhibitor therapy or adoptive cell therapy, clinical benefits are still quite limited [5–7]. One of the causes of this limitation stems from the fact that immunotherapy crucially depends on the localization of immune cells inside solid tumors. In fact, a higher density of cytotoxic T cells inside the tumor is considered as a marker for good prognosis across different cancer types [8–13].

The infiltration of immune actors such as T cells into the tumors is often restricted by different barriers posed by the tumor (cytokines and chemokines secreted by cancer cells [14–17]) or by the tumor micro-environment (collagen fiber density

[18], collagen fiber orientation [19], tumor associated macrophages [20], cancer associated fibroblasts [21] and other cells in the extra cellular matrix [22]). Depending on the infiltration of T cells in the periphery and core of the solid tumors, tumors can be classified as immune-active or hot (higher density of T cells both in the periphery and core), immune-excluded (higher density of T cells in the periphery, lower density in the core) and cold (lower density of T cells both in the periphery and core) tumors [23–25].

The primary recruitment of immune cells in the periphery of tumor depends on chemoattraction towards different chemokines and/or cytokines secreted by the cancer cells or and/or immune cells themselves [26, 27]. To infiltrate inside the tumor some type of persistence of the immune cells is needed. Antigenic stimulus promotes this persistence [25]. The function of these cells (destruction of cancer cells) depends on the target antigen expressed by the

cancer cells but infiltration can happen both in antigen positive and negative tumors [28]. The density of immune cells inside the tumor and their detailed spatial arrangement is strongly correlated with the clinical outcome of immunotherapy [29–31].

In this article, we investigate both experimentally and computationally the infiltration of 3D spheroids composed of mouse melanoma cells by P-mel activated splenocytes. A minimal mechanistic computational model captures the measured *in-vitro* immune cell density distribution inside and outside the solid tumor. The effects of activity and proliferation of immune cells on the infiltration process leads to a better understanding of the mechanism of infiltration of tumor by immune cells. This improved understanding may help us overcome immune exclusion and hence improve the clinical efficacy of immunotherapy.

2. Results

2.1. Infiltration of a cancer spheroid by splenocytes

To study how immune cells invade a tumor spheroid, we prepared 3D spheroids from subconfluent mouse melanoma cells, as discussed in the Materials and Methods section. The spheroids were placed in contact with P-mel activated splenocytes (adaptive immune cells isolated from the spleen [28]) and we followed the co-culture using time-lapse confocal microscopy for 20.6 h. Without the activation the splenocytes do not move and invade the tumor. Figure 1(a) shows a typical 3D reconstruction of the 3D spheroid in contact with the splenocytes. The progression of splenocytes inside the tumor is shown in figure 1(b). In order to quantify the infiltration dynamics, we consider individual xy planes and measure the number of pixel occupied by splenocytes as a function both of time and distance from the 3D spheroid boundary, obtained as discussed in the Materials and Methods section (figure 1(c)). Figure 1(d) represents the total number of splenocyte pixels inside and outside the tumor spheroid as a function of time. We also observed a sharp transition in the splenocytes profile near the tumor boundary. The dense layer of splenocytes gradually moves towards the core of the tumor spheroid, keeping the maximum density near the boundary.

The gradual increment of the number of splenocytes inside the spheroid might arise from two factors, (i) the recruitment of the splenocytes inside the tumor from outside and (ii) the proliferation (cell division) of the splenocytes inside the tumor after the initial recruitment. The number of splenocytes outside the tumor spheroid remains almost unaltered (figures 1(c) and (d)), suggesting that the dominant mechanism of infiltration is the proliferation of splenocytes inside the tumor spheroid. In this regard, we note that the splenocytes only divide in presence of cancer cells, and that therefore there is effectively

no division (i.e. a constant number of cells) outside the tumor spheroid. This is a characteristic feature of tumor-infiltrating T cells, as revealed by immuno-histochemistry in colorectal carcinomas where T cell proliferation was found to be higher when T cells are in contact with cancer cells than when in they are in the stroma [32]. To confirm this point for our model system, we carried out experiments in 4 μm pore-size transwells, where the melanoma cells were plated in the well and activated splenocytes were put on the 4 μm pore-size transwell. The cells could exchange factors but were not able to touch each other. We found that all the splenocytes died after 16 h, suggesting that they need contact signals with cancer cells for survival.

2.2. Computer simulation of the infiltration of cancer spheroid by splenocytes in 2D

To simulate the infiltration of tumor by splenocytes, we use the Cellular Potts Model (CPM), where the individual cells are represented by a few lattice points (pixels) occupying a certain area on a single square lattice (detailed in the Materials and Methods section). We consider a confluent domain of cancer cells (green cells, denoted by E) as a circle, (representing a simplified 2D version of the tumor spheroid) of radius 100, surrounded by splenocytes (red cells, denoted by T). The whole simulation uses a simulation box of length 600. Each cell is initially composed of 25 pixels. The target area and target perimeter of the cells are 25. Considering the typical size of a cell, 1 pixel ~ 1 μm. The medium (the empty space which is not occupied by cells, black region) is denoted by m. Figure 2(a) shows the initial configuration of the simulations.

In this approach, the infiltration of the tumor by splenocytes depends on two factors, cell-cell and cell-medium contact energies (J) and the motility of the immune cells. In the original CPM, the motility of the cells arises solely from the fluctuation amplitude (A) of the cell membrane (see Materials and Methods section). We use very small value of the fluctuation amplitude for the E cells ($A_E = 1$) to construct the solid tumor spheroid. We also use $A_T = 1$ for the splenocytes. The diffusive motility arising from the fluctuation amplitude (even for higher values of A_T) is not enough for the splenocytes to invade the solid tumor even at favorable contact energies. We therefore add a directed motility term for the immune cells in the Hamiltonian of the system, where a force (μ) acts on the center of mass of the cells with a directional persistence (τ) (detailed in the Materials and Methods section). This kind of persistent random walk is well known for T cells migration [33–37]. We choose $A_T = 1$ in presence of active motility of T cells. We select values of contact energies ($J_{Em} = 20$, $J_{Tm} = 3$, $J_{EE} = J_{TT} = 6$, $J_{ET} = 1$) and activities of splenocytes ($\mu = 40$, $\tau = 10$), such that the splenocytes can invade the tumor. Later, we will discuss the effect of varying
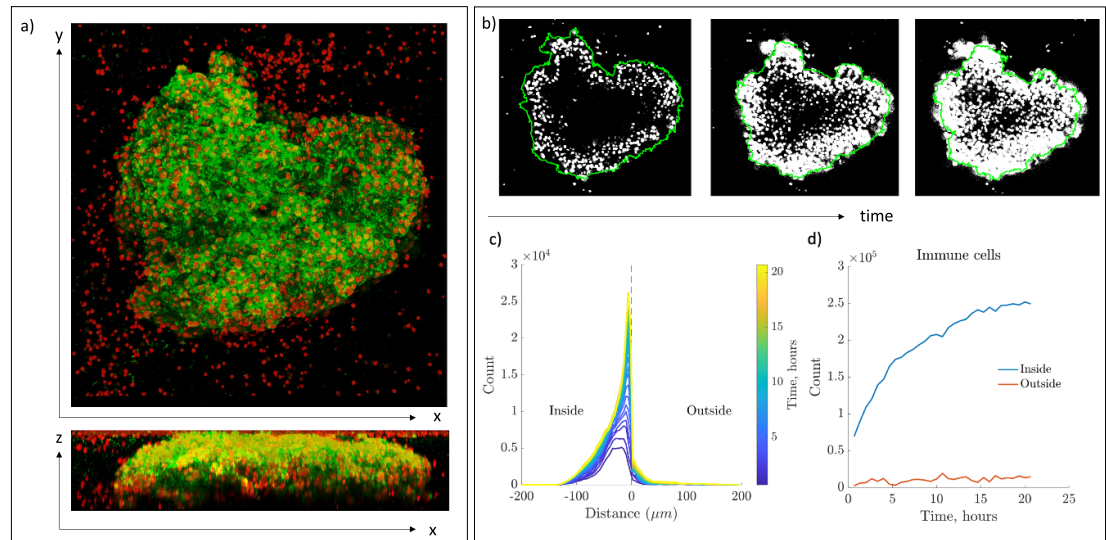
Figure 1. Experimental analysis of splenocyte infiltration of a B16hgp100 mouse melanoma spheroid. 3D spheroids of B16hgp100 mouse melanoma were obtained as described in the experimental methods section. After spheroid seeding, Pmel activated splenocytes were added to the suspension prior to collagen polymerization. Immediately after, cells were time-lapsed images every 40 min for 20.6 h (Nikon Nikon A1 laser scanner confocal (63X) with a z-stack of 1 μm. A 3D reconstruction has been obtained as described in the methods section. (a) The 3D reconstruction of a cancer spheroid composed of B16hgp100 mouse melanoma cells (green) in presence of Pmel activated splenocytes (red). The image corresponds to $t = 0$. (b) Images of a single confocal plane at three different time steps (times are $t = 0$, $t = 400$ and $t = 800$ min) . The splenocyte signal has been thresholded and binarized (white pixels) while the contour of the spheroid is reported in green. The scale bar is 100 μm. (c) The splenocyte front profile as a function of time. The profile is centered around the spheroid boundary and the distance is computed from the boundary. (d) The total number of splenocyte pixels inside and outside the tumor spheroid as a function of time.
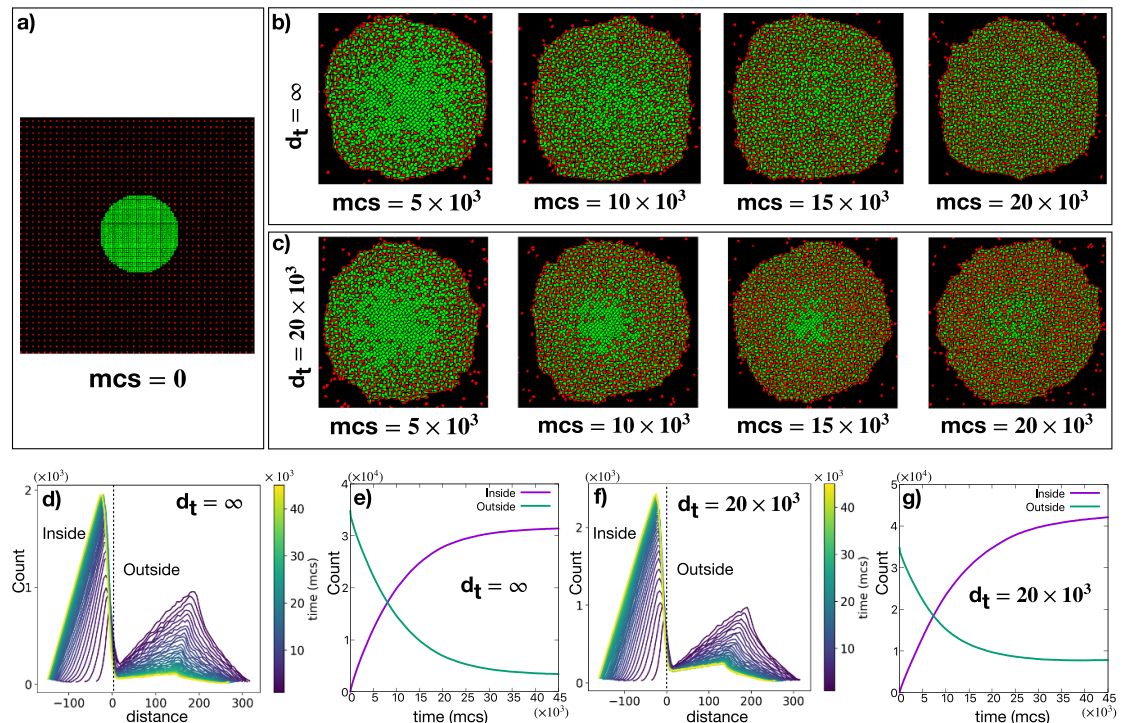

Figure 2. Computer simulation of infiltration of cancer spheroid by splenocytes in 2D. (a) The representative initial configuration of the simulation box composed of green melanoma cells surrounded by red splenocytes. Snapshots of the simulations at different times (mcs), representing the different stages of infiltration of the tumor, (b) in absence any proliferation of splenocytes and (c) considering the proliferation of splenocytes. (d) The splenocyte front profile (centered around the spheroid boundary) as a function of time, in case of no proliferation of splenocytes. (e) The total number of splenocyte pixels inside and outside the tumor spheroid as a function of time, in case of no proliferation of splenocytes. (f) and (g) The similar profiles considering the proliferation of splenocytes. Distance $= 0$ represent the boundary of the tumor spheroid.

these contact energies and activities on the simulated infiltration dynamics.

Figures 2(b) and (c) represent the different stages of infiltration as a function of time without and with proliferation of the splenocytes, respectively. The time is tracked by Monte Carlo steps (mcs), where 1 mcs is defined by $n \times n$ pixel copy attempts ($n \times n$ is the total number of pixels in the system). Comparing with the experimental time scale, 1 mcs ~ 1.65 s. The splenocytes are only allowed to divide if they come into contact with tumor cells. Hence, the splenocytes do not grow and divide outside the tumor. At each mcs, the target area (V_0) of each splenocyte inside the tumor increases with a fixed rate. When the actual area becomes double of the initial target area, the cell will split into two cells each with equal size. The target perimeter (S_0) of the splenocyte is increased by maintaining constant the ratio $S_0 / \sqrt{(V_0)}$. We can quantify the proliferation or division using the target area doubling time of the splenocytes d_t. Due to different environments (pressure exerted by surrounding tumor cells and presence of other splenocytes) and the stochasticity, not all the splenocytes divide together after each d_t mcs. This creates an heterogeneity in the size (area) of the splenocytes at a particular time, as is also observed in the experiments. We choose $d_t = 20 \times 10^3$ (9.1 h) as a baseline. We will discuss later the effect of doubling time on the infiltration dynamics.

We quantify the infiltration dynamics by counting the number of splenocyte pixels inside and outside the tumor as a function of time and distance from the boundary of the tumor. Figures 2(d)–(f), g depict the splenocytes profile in absence ($d_t = \infty$) and presence ($d_t = 20 \times 10^3$) of splenocytes proliferation, respectively. Comparing with the experimental results in (figures 1(c) and (d)), the profiles of the splenocytes from the simulations (figures 2(d)–(g)) are different in the initial stages; in the simulation the tumor spheroid is surrounded by splenocytes which take some time to enter into the tumor, but in the experiment, some splenocytes are already in contact with the tumor at the beginning. Thereafter, we observe qualitatively similar profiles (both inside and outside the tumor) in the case of proliferating splenocytes (figures 1(d) and 2(g)).

Furthermore, the distribution of splenocytes with respect to the distance from the boundary of the tumor closely resembles the experimentally observed distribution. Specifically, the dense layer of splenocytes gradually moves towards the center of the tumor spheroid keeping the maximum density near the boundary. In absence of proliferation ($d_t = \infty$), the number of splenocytes outside the tumor gradually decreases in contrast with the case of proliferating splenocytes, where the number of splenocytes outside the tumor becomes almost constant (as observed in the experiment) at mcs $>25 \times 10^3$. The boundary region of the tumor is filled up by splenocytes

after initial recruitment and proliferation, the lack of physical space do not allow further recruitment of splenocytes inside the tumor from outside and hence the number profile of splenocytes outside the tumor becomes constant.

2.2.1. Effect of varying contact energies

Our computational system is composed of two kind of cells (cancer cells, E and splenocytes, T) and the medium (m). So, we have to specify 5 different kind of contact energies (since $J_{mm} = 0$): J_{Em}, J_{Tm}, J_{EE}, J_{TT} and J_{ET}. We can group them into three surface tension parameters, $\gamma_{Em} = J_{Em} - J_{EE}/2$, $\gamma_{Tm} = J_{Tm} - J_{TT}/2$ and $\gamma_{ET} = J_{ET} - (J_{EE} + J_{TT})/2$. We fix the homotypic cell-cell contact energies ($J_{EE} = J_{TT} = 6$), and vary the surface tensions by varying the heterotypic contact energies (J_{Em}, J_{Tm} and J_{ET}). We also choose, $J_{Tm} = 3$ ($\gamma_{Tm} = 0$), such that the T cells do not strongly cluster together in the medium ($\gamma_{Tm} > 0$ promotes clustering and $\gamma_{Tm} < 0$ prefers individual T cells in the medium) and $J_{Em} = 20$ ($\gamma_{Em} = 17$); a high positive value of γ_{Em} is needed to maintain the compactness of the tumor. We observe change in infiltration dynamics as we vary J_{ET} (or γ_{ET}). We see a significant change in the profile of T cells (splenocytes) with time for $J_{ET} > 3$, where $\gamma_{ET} > 0$ (figure S1 in supplementary material). $\gamma_{ET} < 0$ facilitates tumor infiltration, as it is easier (energetically favorable) for T cells to be in contact with the E cells compared to be in the medium. At higher positive values of J_{ET}, it is very difficult for the T cells to enter into the tumor spheroid. But, due to their active motility (motile force, μ and persistence, τ), a few T cells can still enter into the tumor spheroid, and can then grow and divide inside the tumor. This results in very slow increase in the number of splenocytes inside the tumor.

2.2.2. Effect of splenocytes activity

Another important factor for the infiltration of tumor is the activity of the splenocytes. In the simulation, the activity of the splenocytes (T cells) is determined by the two factors, (i) the active motile force (μ) and (ii) the persistence time of cell polarity (τ). Figures S2 and S3 in supplementary material depict the infiltration dynamics at different values of μ and/or τ. For very low values of μ and/or τ ($\mu = 20$ and/or $\tau = 1$), it is extremely difficult for splenocytes to invade the tumor even with favorable contact energy conditions ($\gamma_{ET} = -2$). At the other extreme, for very higher values of μ and/or τ ($\mu = 50$ and/or $\tau = 30$), the splenocytes release to the medium at later stage of the simulations, by loosening the boundary and/or breaking apart the tumor spheroid. Especially, long persistence times (τ) generate collective migration of T cells, which break apart the tumor spheroid. The intermediate range of μ and/or τ (we use $\mu = 40$ and $\tau = 10$ for all the other 2D simulations in this manuscript) can generate reasonable infiltration dynamics, qualitatively mimicking the experimental results.
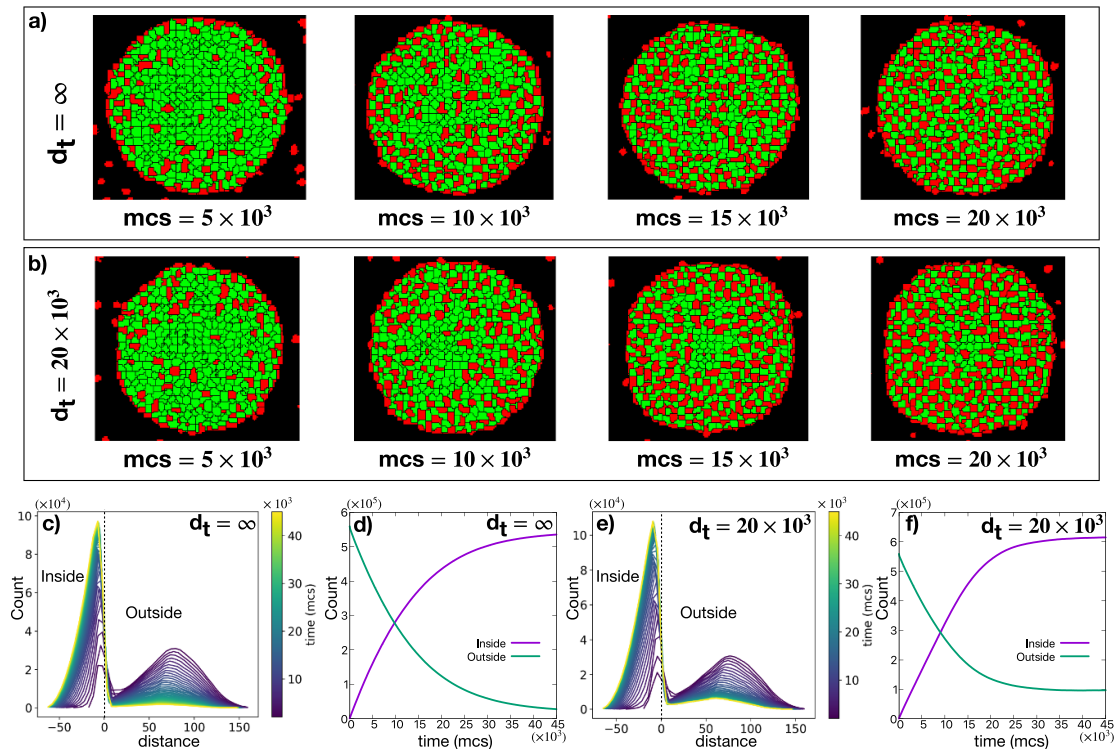
Figure 3. Computer simulation of the infiltration of cancer spheroid by splenocytes in 3D The snapshots (the mid-*xy* plane) of the simulations at different time (mcs), representing the different stage of infiltration of tumor spheroid by splenocytes, (a) in absence any proliferation of splenocytes and (b) considering the proliferation of splenocytes. (c) The splenocyte front profile (centered around the spheroid boundary) as a function of time, in case of no proliferation of splenocytes. (d) The total number of splenocyte pixels inside and outside the tumor spheroid as a function of time, in case of no proliferation of splenocytes. (e) and (f) The similar profiles considering the proliferation of splenocytes.

2.3. Computer simulation of infiltration of cancer spheroid by splenocytes in 3D

In the experimental system, the spheroid is a 3D flattened structure (see figure 1(a)). This motivated us to extend our simulations to 3D. In our 3D simulations, the tumor is a spheroid of radius 50 in a cubic simulation box of length 250. Target volume (similar to area in 2D) and target surface area (similar to perimeter in 2D) of the cells are 125 and 180 respectively. We choose $\mu = 600$ for the splenocyte; the reason for this higher order of magnitude of μ in 3D compared to 2D simulations is that the μ is proportional to the volume (area in 2D) of the cells in our model. All the other parameters are same as in 2D, as described in figure 2. The snapshots (figures 3(a) and (b)) are the mid-xy plane of the 3D simulation box. We found qualitatively similar infiltration dynamics (figures 3(c)–(f)) as observed in 2D (figures 2(d)–(g)).

2.3.1. Comparison of the shape of the splenocytes profile between 2D and 3D simulations
The distributions of splenocytes with respect to distance trail off inside the tumor more sharply in case of 2D (figures 2(d) and (f)) than in 3D (figures 3(c) and (e)). This slower drift of the profile of splenocytes is closer to what was observed in the experiment

(figure 1(c)). This is a not unexpected consequence of dimensionality. In case of 2D, the number of splenocytes inside the tumor should be proportional to the distance, whereas it is proportional to the distance^2 in 3D, once the area (2D) or volume (3D) of the tumor is filled up by splenocytes. We find almost linear relationships with respect to distance inside the tumor (at least in the later stages of the simulations), by rescaling the distributions with 1/distance in 2D (figures S4(a) and (b) in supplementary material) and 1/distance^2 in 3D (figures S4(c) and (d) in supplementary material). Also, the area (volume in 3D) of the tumor spheroid slowly increases with time to accommodate the splenocytes inside the confluent layer of the tumor cells. This change in volume does not seem to occur in the experiment, as the tumor spheroid there is somewhat subconfluent, which can therefore accommodate splenocytes without changing the volume significantly.

We also calculated the splenocytes profile with respect to distance from the boundary of the 3D spheroid by dividing the 3D simulation box in 2D layers along the *z*-axis and obtain the histogram for each 2D layer and finally summing them to construct the whole distribution. This was the method used to analyze the experiment (detailed in the Materials and Methods section). We found similar distributions

(figure S5 in supplementary material) as compared to figures 3(c) and (e), although the method of calculation is different. In case of figures 3(c) and (e) the distance represents the radial distance (R) from the boundary of the sphere, whereas in figure S5 in supplementary material the distance represent the combination of radius (r) of each circular disc. The distribution is similar inside the tumor because of the spherical geometry of tumor. As we have seen previously, for each 2D circle the distribution $\sim r$, and

thus the combined distribution should be $\sim \sum r_i \sim$ distance^2.

2.4. Contact dependent growth

As previously discussed, the splenocytes can only grow and divide if they are in contact with the cancer cells. To generalize the above simulations, We next assumed that the growth of the T cells would stop below a varying fraction of contact between T and E cells. We quantified this contact between E and T cells by a parameter f defined as:

$$f = \frac{\text{shared perimeter (surface area in 3D) between one T cell and surrounding E cells}}{\text{perimeter (surface area in 3D) of that T cell}}$$

We observed that the boundary of the tumor become more ragged and the splenocytes start to release to the medium (outside the tumor) for $f < 0.90$ (figure 4(a)) both in 2D and 3D. The sharpness of the transition of the splenocytes profile near the tumor boundary decreased. This feature is also evident from the number of splenocytes as a function of time (figures 4(a) and (b)). The number of splenocytes outside the tumor starts to increase at long time (instead of saturating). So, for a controlled division of splenocytes (as observed in the experiment), we need a relatively high value of f. Unless otherwise stated, We use $f = 0.95$ for all the simulations in this manuscript. In principle, another way to inhibit excessive growth is to change the baseline growth rate depending on the pressure the splenocytes feel (adding a direct dependence of pressure on doubling time of splenocytes, d_t) due the presence of other cancer cells and splenocytes. Here, we only considered a constant growth rate of the splenocytes and control their proliferation depending on the contact with other cancer cells, since this is important for survival and growth of the splenocytes.

2.5. Effect of doubling time of splenocytes

The rate of cell division of splenocytes (T cells) is highly uncertain, with estimates in the literature differing by almost an order of magnitude (from few hours to days) [38, 39]. It depends on the type of antigenic stimulus [40] and the time of activation [39]. At the peak of cell division, fully activated pmel-1 T cells with FP-hgp100 and IL2 can divide at a rate of approximately 5.3 h cell^{-1} division and later it decreases to 12.7 h cell^{-1} division [41]. We have therefore studied this process with varying division rates.
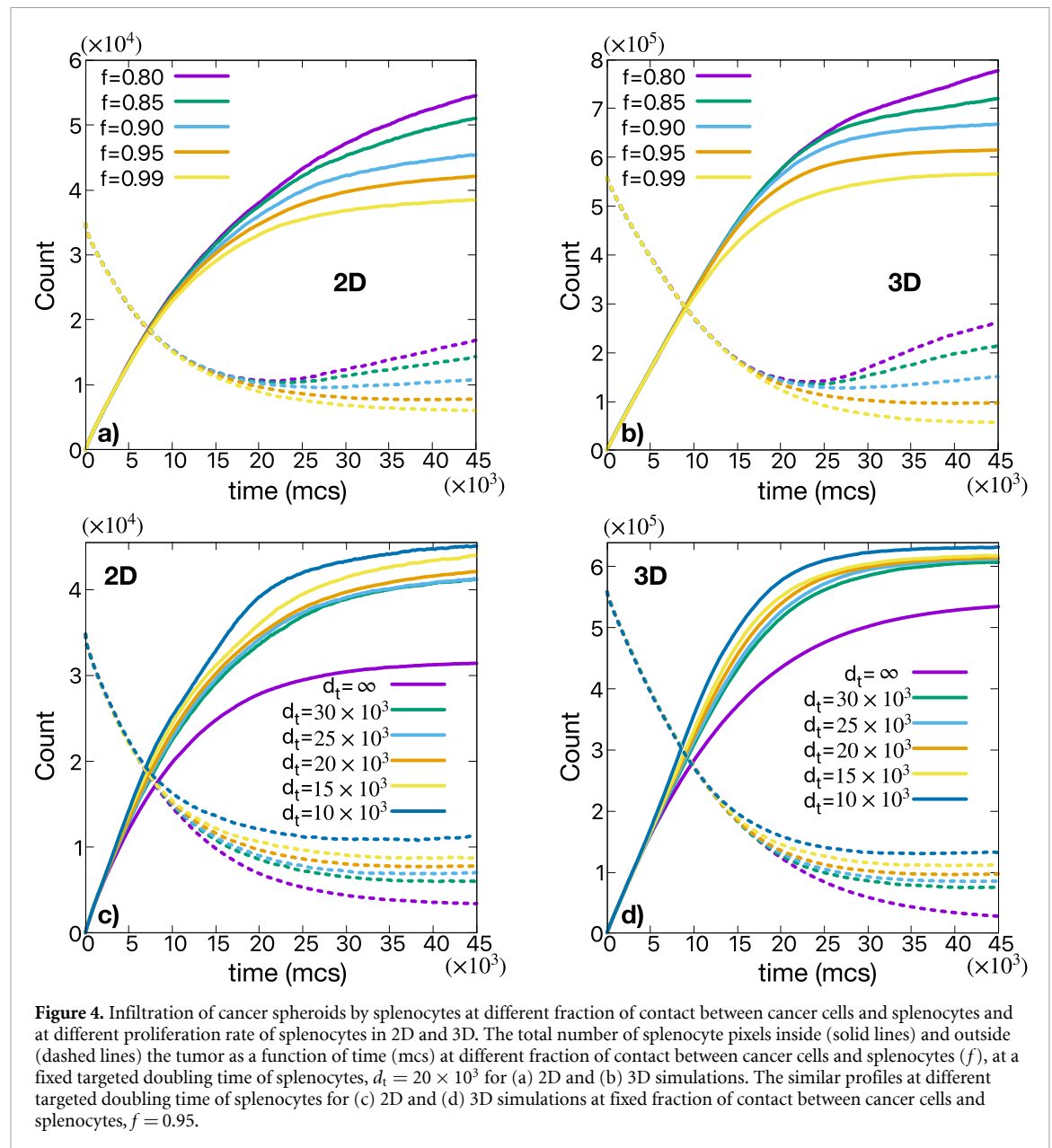
Although, we choose doubling time of splenocytes $d_t = 20 \times 10^3$ in the previous analysis, the infiltration dynamics remains qualitatively similar for different reasonable choice of d_t, as shown in figures 4(c)

and (d). Of course, the infiltration slows down when d_t increases. The rapid division of splenocytes at smaller values of d_t fills up the boundary region of the tumor very quickly, which do not allow splenocytes to enter further into the tumor spheroid, so the number of splenocytes outside the tumor saturates at higher values.

2.6. Effects of cell rigidity

For fixed contact energies and activity of the splenocytes, the rigidity of the tumor cells can affect the infiltration dynamics. Here, we vary the rigidity of the cells by changing their strength of the perimeter (surface area in 3D) constraint (λ_S). The infiltration profile is mainly affected due to two reasons: (i) the recruitment and movement of the splenocytes inside the tumor and (ii) the proliferation of the splenocytes.

Changing the rigidity of the tumor cells (λ_S^E) affects the proliferation of the splenocytes. The growth of the splenocytes is affected by the high pressure of the surrounding very rigid tumor cells. We observe gradual slowing down of the infiltration dynamics and decrease in number of splenocytes inside the tumor as we increase the rigidity of the cancer cells (figure 5). The slower infiltration rate is due to both the slower movement and proliferation of splenocytes inside the rigid tumor, but the numbers of splenocytes inside the tumor start to saturate to smaller values mainly due to the slower proliferation rate. A similar observation was found in case of changing the doubling time d_t (figures 4(c) and (d)). We also verified this conclusion by conducting simulations without proliferation ($d_t = \infty$) and finding that the infiltration dynamics is not affected much with changes in λ_S^E especially for $\lambda_S^E \leqslant 2.0$. This rigidity dependent infiltration dynamics will be interesting to test by experimentally studying tumor composed of cells with different rigidity.

Figure 4. Infiltration of cancer spheroids by splenocytes at different fraction of contact between cancer cells and splenocytes and at different proliferation rate of splenocytes in 2D and 3D. The total number of splenocyte pixels inside (solid lines) and outside (dashed lines) the tumor as a function of time (mcs) at different fraction of contact between cancer cells and splenocytes (f), at a fixed targeted doubling time of splenocytes, $d_t = 20 \times 10^3$ for (a) 2D and (b) 3D simulations. The similar profiles at different targeted doubling time of splenocytes for (c) 2D and (d) 3D simulations at fixed fraction of contact between cancer cells and splenocytes, $f = 0.95$.

3. Discussion

In this paper, we studied experimentally and computationally the spatial distribution of infiltrating immune cells inside a tumor cell spheroid as a function of time. This is an issue of direct relevance for a better understanding of the conditions under which immunosurveillance and immunotherapy is likely to be beneficial [19, 24, 42]. We find that infiltration is dominated by the proliferation of the splenocytes which is stimulated by contact with cancer cells. In our computational model, we incorporated a dependence of proliferation rate on contact between cancer and immune cells and with this assumption we were able to explain the experimentally observed T cell density profile. In the model, we did not consider immune cell death, as no cell death is observed during the experimental time.

We demonstrated that the contact energies and activity of splenocytes are deciding factors governing the infiltration dynamics. Chemotaxis of immune cells due to several chemokines secreted by cancer cells or T cells can also be an important factor towards the infiltration dynamics. Chemotaxis is important for rapid recruitment of distal T cells [27] into the tumor, local T cell density inside the tumor is amplified by proliferation [26, 28]. In the present experiment, splenocytes are already in contact with the tumor. So, the distal recruitment process is not important here.

Our computational model predicts that the active motility of the immune cells is required for both the initial recruitment and movement of splenocytes inside the tumor. An intermediate range of activity (active motile force, μ and persistence, τ) is needed to protect the compactness of the tumor spheroid
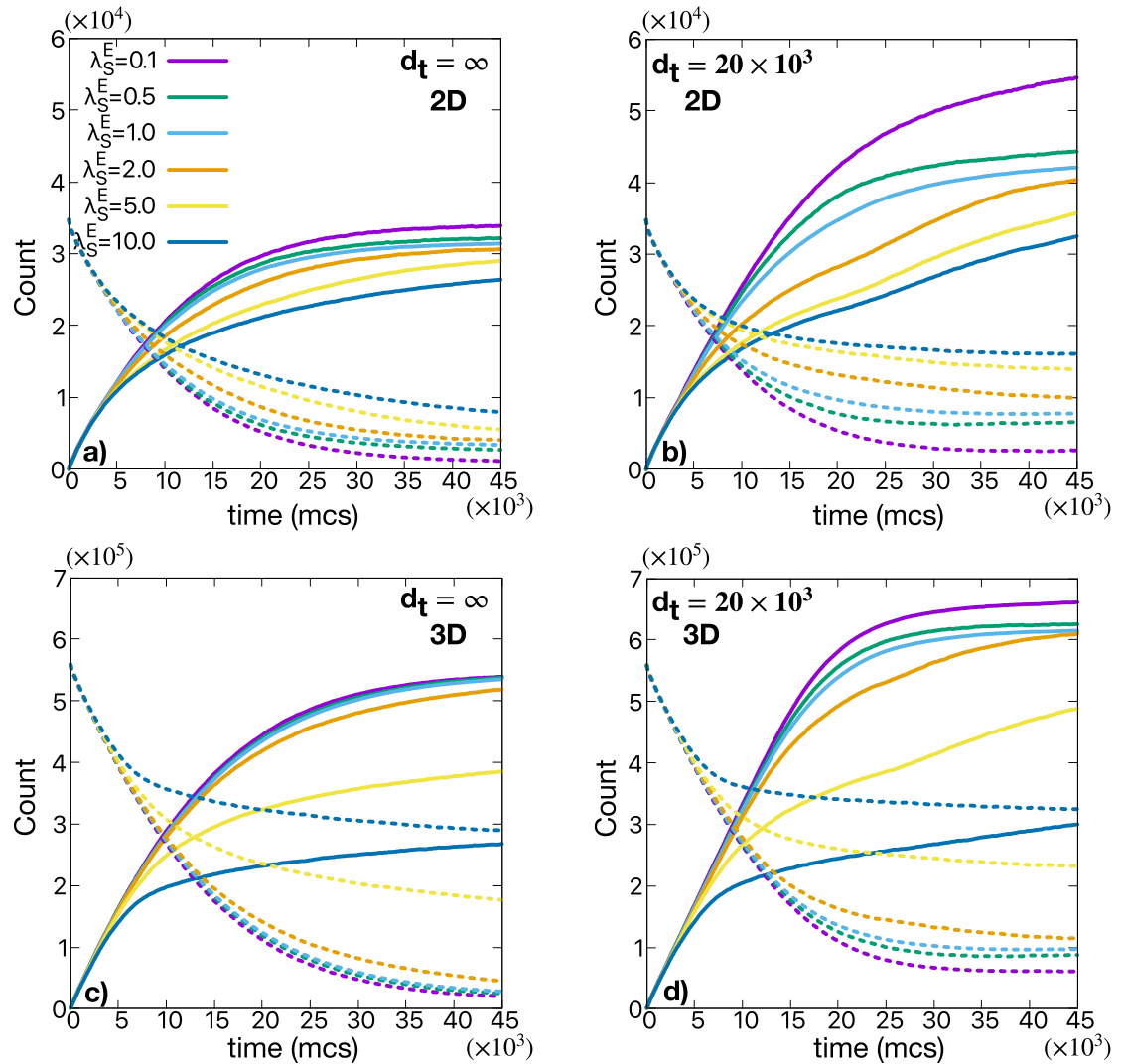
Figure 5. Infiltration of cancer spheroids by splenocytes with varying rigidity of tumor cells (λ_S^E) in 2D and 3D. The total number of splenocyte pixels inside (solid lines) and outside (dashed lines) the tumor as a function of time (mcs) at different rigidity of tumor cells (λ_S^E) (a) for no proliferation of splenocytes ($d_t = \infty$) and (b) considering proliferation of splenocytes (at a fixed targeted doubling time of splenocytes, $d_t = 20 \times 10^3$) in case of 2D simulations. (c), (d) The similar profiles in case of 3D simulations.

and mimic the experimental infiltration dynamics. This finding could have implications for the behavior of 'exhausted' T-cells as well as the possible role of nutrient availability, in the context of modern immunotherapy.

Increasing tumor cell rigidity interferes with T-cell infiltration. One can also map out how the rates and patterns of infiltration vary with the strength of various types of cell-cell adhesion. Obviously, these findings need to be checked against a new generation of experiments that allow for manipulation of these cellular properties. Future work will determine whether our approach is flexible enough to encompass a variety of different systems and different measurement protocols, see e.g. [43, 44]

The current study focuses only on the infiltration of splenocytes inside a *in vitro* tumor spheroid. Future extensions are needed to take into different tumor micro-environmental factors, such as density

and orientation of collagen fiber [19], other contributing cells in extracellular matrix [45], and/or different competing chemical environments [46] which restrict the immune cell infiltration.

4. Materials and methods

4.1. Cell culture

B16hgp100 cell line [28] were cultured in RPMI 1640 medium (cod.32404014, Thermo Scientific) supplemented with 10% FBS, (Penicillin/Streptomycin; cod. ECB3001D, EuroClone, Italy), 2 mM Glutamax (cod. 35050061, Thermo FischerScientific), 1% Non Essential Aminoacids (NEA; cod. ECB3054D, EuroClone, Italy), 1 mM Sodium Piruvate (cod. ECM0542D, EuroClone, Italy), 0.055 mM 2-Mercaptoethanol (cod. M3148, Sigma Aldrich-Merck Millipore, Germany), 10 μg ml^{-1} Blasticidin S (cod. 15205, Sigma Aldrich-Merck Millipore, Germany)

at 37°, 5% CO2 and 95% humidity. Activated Pmel splenocytes were cultured in standard condition in RPMI 1640 medium (cod. 32404014, Thermo Scientific) supplemented with 10% FBS (cod.ECS0180D, EuroClone, Italy), 1% antibiotics (Penicillin/Streptomycin; cod. ECB3001D, EuroClone, Italy), 2 mM Glutamax (cod. 35050061, Thermo Fischer Scientific), 1% Non Essential Aminoacids (NEA; cod. ECB3054D, EuroClone, Italy), 1 mM Sodium Piruvate (cod.ECM0542D, EuroClone, Italy), 0.055 mM 2-Mercaptoethanol (cod.M3148, Sigma Aldrich-Merck Millipore, Germany) , 10 μg ml^{-1} IL-2 (cod. I0523, Sigma Aldrich-Merck Millipore, Germany) at 37°, 5% CO2 and 95% humidity. Cells were stimulated with 1 μM Pmel antigen (cod. APREST87051, Sigma Aldrich-Merck Millipore, Germany) every 72 h for a week before the experiment [47]. B16hgp100 cells and Pmel splenocytes were kindly provided by Dr Luca Gattinoni (Regensburg Center for Interventional Immunology: Regensburg, DE).

4.2. 3D spheroids formation, confocal imaging and image analysis

B16hgp100 multicelullar spheroids were obtained from subconfluent cells using the hanging-drop technique [48].Briefly, B16hgp100 cells were harvested by trypsinization and then properly resuspended (10 cells μ^{-1}) in 2% methylcellulose (cod. M6385, Sigma Aldrich-Merck, Germany) in complete actived Pmel splenocytes medium supplemented with 1 mg ml^{-1} IFN-γ (cod. I4777, Sigma Aldrich-Merck, Germany) for 72 h.50 μl drops of cell suspension (500 total cells) were seeded onto the lid of a 100 mm Petri dish and the bottom of the dish rinsed with 10 ml of PBS 1x acting as a hydration chamber. After spheroids seeding, the lid was inverted onto the PBS-filled bottom chamber and incubated for 72 hr days at 37°, 5% CO2 and 95% humidity to allow spheroids formation.

Two hours before the start of the time-lapse acquisitions, both 3D spheroids and activated P-mel splenocytes were labeled with 1 μM SIR-Actin probe for F-actin (cod.SC001, Spirochrome) and 1 μM SPY505-DNA probe (cod.SC101 Spirochrome), respectively. Then, single spheroids (one for each well of a μ-Slide ; cod. 81506, Ibidi) were embedded in non-pepsinzed rat-tail collagen type I solution (2.5 mg ml^{-1}; cod. C3867, Sigma Aldrich-Merck, Germany) and activated Pmel splenocytes (2×10^6 cells/well) added to the suspension , prior to collagen polimerization (37° for 10 min). Immediately after, cells were time-lapse imaged every 40 min for 20.6 hr using a Nikon A1 laser scanner confocal (63X) with a *z*-stack of 1 μm.

We process 2D layers of the 3D confocal images one by one. At first, we use a segmentation algorithm to define the border of the cancer spheroid. Next, for each pixel that belongs to a splenocyte, we find the

distance to the boundary. The distance is negative if the pixel is inside the boundary and positive otherwise. A histogram—simple count—is constructed at each time step. Finally, the histograms are summed over the layers and a colormap where color represents time is produced.

4.3. Transwell co-culture

B16hgp100 cells were plated 20 000 cells cm^{-2} into each well of 12-well plate. The next day, murine melanoma cells were washed with PBS ,put in fresh growth medium and activated Pmel splenocytes (2×10^6 cell/ insert) were placed onto 4 μm pore-size transwell insert in complete growth medium with the addition 10 μg ml^{-1} IL-2 (cod. I0523, Sigma Aldrich-Merck Millipore, Germany) and 1 μM Pmel antigen (cod. APREST87051, Sigma Aldrich-Merck Millipore, Germany) for 16 hr.

4.4. Computational model

The dynamics of the cells is generated by CPM using an open source software CompuCell3D [49]. The cells reside on a single 3D square cell lattice. Each lattice site (voxel) is denoted by a vector of integers $\vec{i}$. The cells are extended objects occupying several voxels. The cell index of the cell occupying voxel $\vec{i}$ is denoted by $c(\vec{i})$ and the type of the cell is denoted by $t(c(\vec{i}))$. Many cells can share the same cell type. The Hamiltonian of the system is described as:

$$H = H_{\text{contact}} + H_{\text{vol}} + H_{\text{sur}}$$

where,

$$H_{\text{contact}} = \sum_{(\vec{i},\vec{j})\text{neighbors}} J_{t(c(\vec{i})),t(c(\vec{j}))}[1 - \delta_{c(\vec{i}),c(\vec{j})}]$$

$$H_{\text{vol}} = \sum_c \lambda_{\text{V}}(t(c))[V(t(c)) - V_0(t(c))]^2$$

$$H_{\text{sur}} = \sum_c \lambda_{\text{S}}(t(c))[S(t(c)) - S_0(t(c))]^2$$

J denotes the contact energy or adhesion between two cells, the volume (V) and surface area (S) of the cells are constrained by the targeted volume V_0 and targeted surface area S_0 respectively, where λ_{V} and λ_{S} set their strength. The medium (m) is the empty volume of the simulation box which is not filled by the cells. The medium is treated as a special cell type with unconstrained volume and surface area.

In case of 2D simulations, the simulation box is consist of a 2D square lattice and each lattice points is called pixels. The volume and surface area of the cells are actually area and perimeter of the cells respectively in 2D.

The dynamics is generated by changing energy (ΔH) with attempts at copying the lattice site from the neighboring cells/medium, using a modified Metropolis algorithm, with the probability $P =$

$\{\exp(-\Delta H/A : \Delta H > 0; 1 : \Delta H \leqslant 0)\}$. Here, A is a measure of intrinsic activity of the cells giving rise to cell membrane fluctuations. The time is tracked by mcs, where 1 mcs is defined by $n \times n$ voxel copy attempts ($n \times n$ is the total number of voxels in the system). We simulate the system in a square lattice. Nearest-neighbors and second-nearest neighbors have been used to calculate the energy.

To define into account the self-propelled nature or active motility of the cells we incorporate an additional term in the Hamiltonian, H_{motility}, defined as [50–52]:

$$H_{\text{motility}} = -\sum_c \mu_c \hat{n}_c . \vec{r}_c$$

where, μ denotes the motile force acting on the center of mass of the cells and $\hat{n}$ describes the direction of polarity of the cells, which is updated by the rule:

$$\hat{n}_c(\text{mcs}) = \frac{< \vec{v}_c(\text{mcs}) >_{[\text{mcs}-\tau,\text{mcs}]}}{|< \vec{v}_c(\text{mcs}) >_{[\text{mcs}-\tau,\text{mcs}]}|}$$

where, τ is the persistence time of cell polarity, and $\vec{v}$ is the velocity of a cell's center of mass.

Parameters for all the figures described in the manuscript are listed in table S1 in supplementary material.

4.5. Statistics

Figure 1 shows a representative example of two independent experiments yielding similar results. Each figure described in the computer simulation part is averaged over 100 independent simulations.

Data availability statement

All data that support the findings of this study are included within the article (and any supplementary files). Scripts to analyze the confocal microscopy images for tumor spheroid invasion used for the paper are available in https://github.com/ComplexityBiosystems/Spheroid-invasion and the sample code for the computer simulations is provided in https://github.com/mrinmoy169/Spheroid-invasion.

Acknowledgments

Authors' contributions

C A M L P designed experiments. C A M L P and M C L performed experiments. O C and S Z analyzed experimental data. M M and H L designed the model. M M performed simulations and analyzed data. M M and H L wrote the paper with inputs from all authors.

Conflict of interests

We declare we have no competing interests.

ORCID iDs

Mrinmoy Mukherjee ⬤ https://orcid.org/0000-0003-4927-2464
Oleksandr Chepizhko ⬤ https://orcid.org/0000-0003-3001-0827
Maria Chiara Lionetti ⬤ https://orcid.org/0000-0002-5099-2592
Stefano Zapperi ⬤ https://orcid.org/0000-0001-5692-5465
Caterina A M La Porta ⬤ https://orcid.org/0000-0002-3010-8966
Herbert Levine ⬤ https://orcid.org/0000-0002-8819-9055

References

[1] Martínez-Lostao L, Anel A and Pardo J 2015 How do cytotoxic lymphocytes kill cancer cells? *Clin. Cancer Res.* **21** 5047

[2] Calí B, Molon B and Viola A 2017 Tuning cancer fate: the unremitting role of host immunity *Open Biol.* **7** 170006

[3] Turan T *et al* 2018 Immune oncology, immune responsiveness and the theory of everything *J. ImmunoTher. Cancer* **6** 50

[4] Reticker-Flynn N E and Engleman E G 2020 Cancer systems immunology *eLife* **9** e53839

[5] Ager A, Watson H, Wehenkel S C and Mohammed R 2016 Homing to solid cancers: a vascular checkpoint in adoptive cell therapy using CAR T-cells *Biochem. Soc. Trans.* **44** 377

[6] Morotti M *et al* 2021 Promises and challenges of adoptive t-cell therapies for solid tumours *Br. J. Cancer* **124** 1759

[7] George J T and Levine H 2021 Implications of tumor-immune coevolution on cancer evasion and optimized immunotherapy *Trends Cancer* **7** 373

[8] Mahmoud S M, Paish E C, Powe D G, Macmillan R D, Grainge M J, Lee A H, Ellis I O and Green A R 2011 Tumor-infiltrating cd8+ lymphocytes predict clinical outcome in breast cancer *J. Clin. Oncol.* **29** 1949

[9] Sato E *et al* 2005 Intraepithelial cd8+ tumor-infiltrating lymphocytes and a high cd8+/regulatory t cell ratio are associated with favorable prognosis in ovarian cancer *Proc. Natl Acad. Sci.* **102** 18538

[10] Sharma P *et al* 2007 Cd8 tumor-infiltrating lymphocytes are predictive of survival in muscle-invasive urothelial carcinoma *Proc. Natl Acad. Sci.* **104** 3967

[11] Galon J *et al* 2006 Type, density and location of immune cells within human colorectal tumors predict clinical outcome *Science* **313** 1960

[12] Carstens J L, Correa de Sampaio P, Yang D, Barua S, Wang H, Rao A, Allison J P, LeBleu V S and Kalluri R 2017 Spatial computation of intratumoral t cells correlates with survival of patients with pancreatic cancer *Nat. Commun.* **8** 15095

[13] Pagès F *et al* 2018 International validation of the consensus immunoscore for the classification of colon cancer: a prognostic and accuracy study *Lancet* **391** 2128

[14] Oelkrug C and Ramage J M 2014 Enhancement of T cell recruitment and infiltration into tumours *Clin. Exp. Immunol.* **178** 1

[15] Yam A O and Chtanova T 2019 The ins and outs of chemokine-mediated immune cell trafficking in skin cancer *Front. Immunol.* **10** 386

[16] Zhang Y, Guan X-Y and Jiang P 2020 Cytokine and chemokine signals of t-cell exclusion in tumors *Front. Immunol.* **11** 594609

[17] Kohli K, Pillarisetty V G and Kim T S 2022 Key chemokines direct migration of immune cells in solid tumors *Cancer Gene Therapy* **29** 10

[18] Kuczek D E *et al* 2019 Collagen density regulates the activity of tumor-infiltrating t cells *J. ImmunoTher. Cancer* **7** 68

[19] Sun X *et al* 2021 Tumour DDR1 promotes collagen fibre alignment to instigate immune exclusion *Nature* **599** 673

[20] Fridman W H, Pagès F, Sautès-Fridman C and Galon J 2012 The immune contexture in human tumours: impact on clinical outcome *Nat. Rev. Cancer.* **12** 298

[21] Gunaydin G 2021 Cafs interacting with tams in tumor microenvironment to enhance tumorigenesis and immune evasion *Front. Oncol.* **11** 668349

[22] Joyce J A and Fearon D T 2015 T cell exclusion, immune privilege and the tumor microenvironment *Science* **348** 74

[23] van den Bulk J, Verdegaal E M and de Miranda N F 2018 Cancer immunotherapy: broadening the scope of targetable tumours *Open Biol.* **8** 180037

[24] Li X, Gruosso T, Zuo D, Omeroglu A, Meterissian S, Guiot M-C, Salazar A, Park M and Levine H 2019 Infiltration of cd8+ t cells into tumor cell clusters in triple-negative breast cancer *Proc. Natl Acad. Sci.* **116** 3678

[25] Pai S I, Cesano A and Marincola F M 2020 The paradox of cancer immune exclusion: immune oncology next frontier *Tumor Microenvironment* (Cham: Springer International Publishing) pp 173–95

[26] Antonioli L, Blandizzi C, Pacher P, Guilliams M and Haskó G 2019 Rethinking communication in the immune system: The quorum sensing concept *Trends Immunol.* **40** 88

[27] Galeano Niño J L *et al* 2020 Cytotoxic t cells swarm by homotypic chemokine signalling *eLife* **9** e56554

[28] Palmer D C *et al* 2004 Vaccine-stimulated, adoptively transferred cd8+ t cells traffic indiscriminately and ubiquitously while mediating specific tumor destruction *J. Immunol.* **173** 7209

[29] Yuan Y 2015 Modelling the spatial heterogeneity and molecular correlates of lymphocytic infiltration in triple-negative breast cancer *J. R. Soc. Interface* **12** 20141153

[30] Kather J N *et al* 2018 Topography of cancer-associated immune cells in human solid tumors *eLife* **7** e36967

[31] Yu C *et al* 2021 Physics approaches to the spatial distribution of immune cells in tumors *Rep. Prog. Phys.* **84** 022601

[32] Golby S, Chinyama C and Spencer J 2002 Proliferation of t-cell subsets that contact tumour cells in colorectal cancer *Clin. Exp. Immunol.* **127** 85

[33] Beltman J B, Marée A F, Lynch J N, Miller M J and de Boer R J 2007 Lymph node topology dictates T cell migration behavior *J. Exp. Med.* **204** 771

[34] Ariotti S *et al* 2012 Tissue-resident memory cd8+ t cells continuously patrol skin epithelia to quickly recognize local antigen *Proc. Natl Acad. Sci.* **109** 19739

[35] Niculescu I, Textor J and de Boer R J 2015 Crawling and gliding: a computational model for shape-driven cell migration *PLOS Comput. Biol.* **11** 1

[36] Read M N, Bailey J, Timmis J and Chtanova T 2016 Leukocyte motility models assessed through simulation and multi-objective optimization-based model selection *PLoS Comput. Biol.* **12** 1

[37] Esfahani P, Levine H, Mukherjee M and Sun B 2022 Three-dimensional cancer cell migration directed by dual mechanochemical guidance *Phys. Rev. Res.* **4** L022007

[38] Macallan D C, Busch R and Asquith B 2019 Current estimates of t cell kinetics in humans *Curr. Opin. Syst. Biol.* **18** 77

[39] Lewis D A and Ly T 2021 Cell cycle entry control in naïve and memory cd8+ t cells *Front. Cell Dev. Biol.* **9** 727441

[40] Yoon H, Kim T S and Braciale T J 2010 The cell cycle time of cd8+ t cells responding *in vivo* is controlled by the type of antigenic stimulus *PLoS One* **5** 1

[41] Hwang L N, Yu Z, Palmer D C and Restifo N P 2006 The *In vivo* expansion rate of properly stimulated transferred CD8+ T cells exceeds that of an aggressively growing mouse tumor *Cancer Res.* **66** 1132

[42] Fridman W H, Galon J, Dieu-Nosjean M-C, Cremer I, Fisson S, Damotte D, Pagès F, Tartour E and Sautes-Fridman C 2011 Immune infiltration in human cancer: prognostic significance and disease control *Cancer Immunology and Immunotherapy* p 1

[43] Dekkers J F *et al* 2023 Uncovering the mode of action of engineered t cells in patient cancer organoids *Nat. Biotechnol.* **41** 60

[44] Ao Z *et al* 2022 Microfluidics guided by deep learning for cancer immunotherapy screening *Proc. Natl Acad. Sci.* **119** e2214569119

[45] Desbois M and Wang Y 2021 Cancer-associated fibroblasts: key players in shaping the tumor immune microenvironment *Immunol. Rev.* **302** 241

[46] Qin R, Peng W, Wang X, Li C, Xi Y, Zhong Z and Sun C 2021 Identification of genes related to immune infiltration in the tumor microenvironment of cutaneous melanoma *Front. Oncol.* **11** 615963

[47] Klebanoff C A *et al* 2004 Il-15 enhances the *in vivo* antitumor activity of tumor-reactive cd8+ t cells *Proc. Natl Acad. Sci.* **101** 1969–74

[48] Lehmann S *et al* 2017 Hypoxia induces a hif-1-dependent transition from collective-to-amoeboid dissemination in epithelial cancer cells *Curr. Biol.* **27** 392

[49] Swat M H, Thomas G L, Belmonte J M, Shirinifard A, Hmeljak D and Glazier J A 2012 Multi-scale modeling of tissues using compucell3d *Computational Methods in Cell Biology* (*Series Methods in Cell Biology* vol 110) ed A R Asthagiri and A P Arkin (New York: Academic) ch 13, pp 325–66

[50] Kabla A J 2012 Collective cell migration: leadership, invasion and segregation *J. R. Soc. Interface* **9** 3268

[51] Hallou A, Jennings J and Kabla A J 2017 Tumour heterogeneity promotes collective invasion and cancer metastatic dissemination *R. Soc. Open Sci.* **4** 161007

[52] Mukherjee M and Levine H 2021 Cluster size distribution of cells disseminating from a primary tumor *PLOS Comput. Biol.* **17** 1

[53] Salmon H, Franciszkiewicz K, Damotte D, Dieu-Nosjean M-C, Validire P, Trautmann A, Mami-Chouaib F and Donnadieu E 2012 Matrix architecture defines the preferential localization and migration of t cells into the stroma of human lung tumors *J. Clin. Invest.* **122** 899